AIAA-2005-0994

AERODYNAMICS OF FAN FLOW DEFLECTORS FOR JET NOISE SUPPRESSION

Tadashi Murayama *
Dimitri Papamoschou †
Feng Liu ‡
University of California, Irvine, California 92697-3975

The present work describes a three-dimensional RANS investigation of the flow around deflector vanes for noise suppression in separate-flow turbofan engines. The vanes are installed in the bypass duct and deflect the bypass plume downward relative to the core plume. This paper considers a single pair of vanes, with NACA0012 airfoil section, installed in a realistically shaped nozzle operating at static conditions. The axial and transverse forces created by the vanes are computed for various vane angles of attack. It it shown that the thrust loss of the bypass stream ranges from 0.04% with the vanes at zero angle of attack to 0.10% for vanes at 8° angle of attack. For an entire engine with bypass ratio of 5, the corresponding losses are approximately 0.03% and 0.08%. The vanes have an impact of less than 0.025% on the nozzle flow coefficient.

Introduction

The Fan Flow Deflection (FFD) technology [1] is tailored for suppression of "large-scale" turbulent mixing noise from aircraft engines. Large-scale mixing noise is the dominant noise source in turbulent jets. The overarching principle of the FFD technology is reduction of the convective Mach number of turbulent eddies that generate intense downward and sideward sound radiation. In a coaxial separate-flow turbofan engine this is achieved by tilting the bypass (secondary) plume by a few degrees downward relative to the core (primary) plume. Mean flow surveys show that the misalignment of the two flows causes a thick, low-speed secondary core on the underside of the high-speed primary flow, especially in the region near the end of the primary potential core which contains the strongest noise sources. The secondary core reduces the convective Mach number of primary eddies, thus hindering their ability to generate sound that travels to the downward acoustic far field.

Tilting of the bypass stream is possible by means of fixed or variable vanes installed near the exit of the bypass duct. Figure 1 depicts the general concept [1]. Subscale experiments at UCI have demonstrated reductions as much as 5 decibels in effective perceived noise level [2]. It is important, however, to also assess the aerodynamic efficiency of this scheme. This paper describes a computational effort to predict the aerodynamic forces generated by the vanes. The shape of the nozzle approximates that of the separate-flow nozzle tested in NASA Glenn Research Center [3, 4]. The size of the nozzle corresponds to that of a full-scale engine producing 50,000 lb of thrust. We examine a generic placement of a single pair of vanes, as illustrated in Fig. 2, with a NACA 0012 airfoil section.

*Graduate student, Member AIAA
†Professor, Associate Fellow AIAA
‡Professor, Associate Fellow AIAA

[1]U.S. Patent Pending

Computational Approach

Numerical Code

The computational fluid dynamics code used here is known as PARCAE and solves the unsteady three-dimensional Reynolds-averaged Navier-Stokes equations on structured multiblock grids using a cell centered finite-volume method with artificial dissipation as proposed by Jameson et al.[5]. Residual smoothing is used to increase stability. Information exchange for flow computation on multiblock grids using multiple CPUs is implemented through the MPI (message passing interface) protocol. The RANS equations are solved using the eddy viscosity type turbulence models. The code contains the

Baldwin-Lomax algebraic model and the $k-\omega$ two-equation model of Wilcox [7]. Multigrid convergence acceleration is also available. In this study, only the steady-state solution is obtained since we are interested in the time-averaged features of the flow. Since we may deal with the possibility of separated flow over the vane airfoils, the $k-\omega$ model was chosen since algebraic models become unreliable for separated flows. Next we summarize the main elements of the code.

The governing equations for the unsteady compressible turbulent flow with a two-equation $k-\omega$ turbulence model are expressed as follows:

$$\frac{\partial}{\partial t}\int_\Omega \mathbf{W}\, d\Omega + \oint_{\partial\Omega} (\mathbf{F}_c - \mathbf{F}_d)\, dS = \int_\Omega \mathbf{S}\, d\Omega \quad (1)$$

The vector $\mathbf{W}$ contains the conservative variables

$$\mathbf{W} = \left\{ \begin{array}{c} \rho \\ \rho u \\ \rho v \\ \rho w \\ \rho E \\ \rho k \\ \rho \omega \end{array} \right\}. \quad (2)$$

The fluxes consist of the inviscid convective fluxes $\mathbf{F}_c$ and the diffusive fluxes $\mathbf{F}_d$. For the convective fluxes we include the pressure term

$$\mathbf{F}_c = \left\{ \begin{array}{ccc} \rho u & \rho v & \rho w \\ \rho uu + p & \rho uv & \rho uw \\ \rho vu & \rho vv + p & \rho vw \\ \rho wu & \rho wv & \rho ww + p \\ \rho Eu + pu & \rho Ev + pv & \rho Ew + pw \\ \rho ku & \rho kv & \rho kw \\ \rho \omega u & \rho \omega v & \rho \omega w \end{array} \right\}. \quad (3)$$

For the diffusive fluxes we have

$$\mathbf{F}_c = \left\{ \begin{array}{ccc} 0 & 0 & 0 \\ \tau_{xx} & \tau_{xy} & \tau_{xz} \\ \tau_{yx} & \tau_{yy} & \tau_{yz} \\ \tau_{zx} & \tau_{zy} & \tau_{zz} \\ \theta_x & \theta_y & \theta_z \\ \mu^* \frac{\partial k}{\partial x} & \mu^* \frac{\partial k}{\partial y} & \mu^* \frac{\partial k}{\partial z} \\ \mu^* \frac{\partial \omega}{\partial x} & \mu^* \frac{\partial \omega}{\partial y} & \mu^* \frac{\partial \omega}{\partial z} \end{array} \right\}, \quad (4)$$

where

$$\mu^* = \mu_L + \sigma^* \mu_T$$

and

$$\theta_x = u\tau_{xx} + v\tau_{xy} + w\tau_{xz} + \mu^* \frac{\partial k}{\partial x}$$

$$\theta_x = u\tau_{xy} + v\tau_{yy} + w\tau_{zy} + \mu^* \frac{\partial k}{\partial y}$$

$$\theta_x = u\tau_{xz} + v\tau_{yz} + w\tau_{zz} + \mu^* \frac{\partial k}{\partial z}.$$

with τ being the stress tensor. The source term is

$$\mathbf{S} = \left\{ \begin{array}{c} 0 \\ 0 \\ 0 \\ 0 \\ 0 \\ \tau_{ij}\frac{\partial u_i}{\partial x_j} - \beta^* \rho\omega k \\ \frac{\alpha\omega}{k}\tau_{ij}\frac{\partial u_i}{\partial x_j} - \beta\rho\omega^2 \end{array} \right\}. \quad (5)$$

In the above equations, the parameters α, β, β^*, and σ^* are closure coefficients for the turbulence model. The equations are discretized in space by a structured hexahedral grid using a cell centered finite-volume method. Artificial dissipation as proposed by Jameson et al.[5] is implemented. Parallelism is achieved through the implementation of MPI (message passing interface) protocol. The computational domain is decomposed into structured sub-divisions. Since within the code each block is considered as a single entity, only flow and turbulence quantities at the block boundaries need to be exchanged. The governing equations are solved explicitly in a coupled manner through a five stage Runge-Kutta scheme. Time accurate solution can be obtained through a fully implicit dual time stepping scheme. Details of the numerical method and implementation of the $k-\omega$ turbulence model can be found in Ref. citeliu96. Several acceleration techniques are implemented. Convergence to steady state is increased by local time stepping. Residual smoothing introduced by Jameson and Baker [6] gives the explicit scheme an implicit character and increases the maximum allowable CFL number thus a larger local time step. Multigrid technique is also implemented.

Computational Grid

The multiblock grid started four fan diameters upstream of the nozzle exit and ended at the nozzle exit of the bypass duct; the external nacelle was not included. Figure 3 shows views of the grid and its topology. Tables 1 and 2 provide the grid sizes for the clean nozzle and the nozzle with vanes, respectively. A symmetric, diametrically-opposing pair of vanes was used. Due to this symmetry, only one half (180°) of the nozzle was modeled. For the clean case, only one zone was necessary; however, the blocks were divided in the axial direction into four blocks of equal cell count to take advantage of PARCAE's parallel processing capability. For each of the cases with vanes installed, a multiblock grid with six zones was constructed. The six zones can be

categorized into two larger regions. Zones 1 through 5 make up the C-grid around the vane in the region near the exit plane. Zone 6 corresponds to the region directly upstream of the C-grid that extends to the nozzle inlet plane. Figure 3 shows the computational mesh and details of the multiblock grid for cases with vanes installed.

In each grid, the points near the solid walls were clustered. It was necessary for the cells near solid surfaces to be sufficiently fine to capture all the features of the boundary layer. The solid walls were specified as no-slip adiabatic boundaries. The points near the trailing edge of the vane were also clustered. For consistency, the same grid system and topology were used for all vane angles of attack. The grid was generated by GridPro (Program Development Company). Identical grid systems were obtained for different attack angles by taking advantage of restarting from a known solution/grid. This also preserved mesh density and therefore overall cell count.

The vane chord length was equal to the exit height of the nozzle, and the vane traling edge was situated 0.25 chord lengths upstream of the nozzle exit. The area-averaged Mach numbers at the planes of the vane leading edge (LE) and trailing edge (TE), without the vane installed, were $M_{\text{LE}} = 0.44$ and $M_{\text{TE}} = 0.76$. The mid-chord Mach number was $M_{\text{MID}} = (M_{\text{LE}} + M_{\text{TE}})/2 = 0.60$. Grids were generated for five angles of attack ranging from 0° to 8° in increments of 2°.

Flow and Boundary Conditions

The flow conditions imposed at the inlet and exit were the same for all cases. At the inlet, a uniform total pressure was specified corresponding to a perfectly expanded Mach number of 0.9 for the nozzle exit flow. The uniformly-imposed total temperature at the inlet was such that the nozzle-exit temperature matched the ambient temperature. At the nozzle exit, the following pressure boundary condition was imposed:

$$\int_{A_e} (p_e - p_a) dA \;=\; 0 \tag{6}$$

In other words, the area-averaged exit pressure matched the ambient pressure. The Reynolds number is 32×10^6 based on fan exit diameter, or 3.2×10^6 based on vane chord length.

Aerodynamic Parameters

We consider a nozzle discharging at static conditions. The nozzle thrust is obtained by integration of the axial momentum and pressure at the nozzle exit,

$$\mathcal{T} \;=\; \int_{A_e} (\rho_e u_e^2 + p_e - p_a) dA \tag{7}$$

Given the boundary condition Eq. 6, this reduces to

$$\mathcal{T} \;=\; \int_{A_e} \rho_e u_e^2 dA \tag{8}$$

The overall lift of the nozzle is obtained by integration of the transverse momentum flux at the nozzle exit

$$\mathcal{L} \;=\; \int_{A_e} \rho_e v_e u_e dA \tag{9}$$

and, assuming small angles, the overall deflection of the plume is

$$\epsilon \;=\; \frac{\mathcal{L}}{\mathcal{T}} \tag{10}$$

The thrust and lift forces were also calculated by integration of the pressures and stresses acting on the vanes and on the nozzle walls. The results were identical to those obtained by Eqs. 8 and 9. For the lift and drag of individual components, such as the vane alone or the nozzle walls alone, the pressures and stresses were integrated over the areas of those components.

Perhaps the most important quantity to emerge from this effort is the thrust loss, defined as

$$\Delta\mathcal{T} \;=\; \mathcal{T} \;-\; \mathcal{T}_{\text{clean}} \tag{11}$$

where subscript "clean" refers to the clean nozzle without vanes.

The vane airfoils studied here are fairly unique in that they are subjected to an *externally imposed favorable pressure gradient.* In other words, because of the convergence of the nozzle, the "frestream" velocity accelerates in the axial direction. Definition of the aerodynamic coefficients becomes problematic as there is no fixed reference condition. Here we select as reference the area-averaged conditions in the plane of the vane leading edge (LE), in the absence of the vane. The pressure coefficient is defined as

$$C_p = \frac{p - p_{\text{LE}}}{q_{\text{LE}}}, \tag{12}$$

the lift coefficient is

$$C_L = \frac{\text{Lift}}{q_{\text{LE}} S}, \tag{13}$$

and the drag coefficient is

$$C_D = \frac{\text{Drag}}{q_{\text{LE}} S} \tag{14}$$

where q is the dynamic pressure and S is the vane planform area.

It is instructive to compare the aerodynamic characteristics of the vane airfoils with those of a two-dimensional airfoil of the same cross section in an infinite freestream, with $M_\infty = M_{\text{LE}}$ and the same Reynolds number based on chord length. This information will provide guidance to a designer who wants to use a certain type of airfoil (whose properties in an infinite freestream have been documented) for the internal vanes. For brevity, we will use the wording "external" for the reference 2D airfoil, "internal" for the vane alone inside the nozzle, and "system" for the combination of vane and nozzle walls.

Results

As mentioned in the earlier section, we will compare the flow field of the vane airfoil with that of an external airfoil with $M_\infty = M_{\text{LE}} = 0.44$. We begin with the Mach number isocontours, shown in Fig. 4. For the internal airfoil, these contours were calculated in the midplane of the vane. Because of the accelerating nozzle flow, there are substantial differences between the flow field of the internal vane airfoil and that of the external case. It is notable that for $\alpha = 8^\circ$ the external airfoil develops a distinct sonic "bubble" on the upper surface a short distance past the leading edge. For the internal airfoil, there is no presence of such a bubble. This suggests that the favorable pressure gradient delays the onset of sonic flow (and its adverse effects on performance) on the airfoil.

The pressure coefficients on the vane surface are plotted in Fig. 5. We notice that C_p on the internal airfoil does not become as negative as that of the external airfoil, which is consistent with the Mach number contours of Fig. 4. In fact, C_p on the upper surface of the internal airfoil is reminiscent of that on supercritical airfoils. Again this indicates that the externally-imposed negative pressure gradient delays wave-drag effects. Even though the C_p distributions for the internal and external airfoils are very different, the areas enclosed by these distributions seem similar. Note that this area is proportional to the lift coefficient.

It is important to also examine the pressure distribution on the nozzle walls, especially the differences caused by insertion of the vane. To obtain an overall assessment, we examine the axial distribution of the circumferentially-averaged pressure and define a pressure coefficient as per Eq. 12. Figure 6 plots the difference in nozzle-wall C_p between the case with vane ($\alpha = 0^\circ$) and the clean case. It is seen that insertion of the vane reduces slightly the pressure on both nozzle walls. On the outer nozzle wall, which has a significant inclination (Fig. 2), this translates into a "thrust" force. Its implication on the force balance of the entire nozzle will become evident below.

The C_L versus α relation for the internal and external airfoils is practically the same, as shown in Fig. 7. The conditions at the vane leading edge thus seem like a good reference point, at least for lift. When we include the lift contribution of the nozzle surfaces the lift curve slope relation does not change significantly. This means that, with the present vane placement, there is no cancellation effect from the nozzle walls and that all the lift force is transmitted to the plume. The lift slope for the system is 0.13 deg^{-1}, which is close to the theoretical value for a 2D airfoil.

We now turn our attention to the drag coefficient C_D. For the external airfoil and for the vane-alone internal airfoil, the drag is calculated by surface integration of pressures and stresses. When we consider the system (vane plus nozzle), the drag is based on the thrust loss given by Eq. 11. Figure 7 plots C_D versus angle of attack for the external airfoil, the vane-alone airfoil, and the system. The predictions for the external airfoil are in line with experimental data for the NACA0012, i.e., $C_D = 0.0044$ for $\alpha = 0^\circ$ and rising to $C_D = 0.014$ for $\alpha = 8^\circ$. The drag coefficient for the vane-alone airfoil is comparatively very large, starting at $C_D = 0.116$ at $\alpha = 0^\circ$ and reaching $C_D = 0.238$ at $\alpha = 8^\circ$. For the entire system, C_D is moderate and about four times that of the external airfoil.

The high C_D of the isolated vane airfoil may be surprising at first but it is simply a consequence of the external favorable pressure gradient. Essentially, this is a hydrostatic problem of an object subjected to a pressure gradient across its length, much like the buoyancy problem. Assuming a constant pressure gradient

$$\frac{dp}{dx} = \frac{p_{\text{LE}} - p_{\text{TE}}}{c} = \text{constant}$$

the hydrostatic drag is readily derived as

$$D_h = \frac{p_{\text{LE}} - p_{\text{TE}}}{c} \mathcal{V} \tag{15}$$

where c is the airfoil chord length, $\mathcal{V}$ is the volume enclosed by the airfoil surface, and p_{LE} and p_{TE} refer to the pressures at the leading and trailing edges of the airfoil, respectively, in the *absence* of the airfoil. Using the low-Mach number approximation to Bernoulli's equation, it can be shown

$$C_{D_h} = \frac{\mathcal{V}}{c^2 h} \frac{(M_{\text{TE}}/M_{\text{LE}})^2 - 1}{1 + (\gamma/2) M_{\text{TE}}^2} \tag{16}$$

where h is the airfoil span. For the NACA four-digit class of symmetric airfoils [9], integration of the self-similar thickness distribution yields $\mathcal{V} = 0.685\ tch$, where t is the airfoil thickness. In this case Eq. 16 becomes

$$C_{D_h} = 0.685\ \frac{t}{c} \frac{(M_{\text{TE}}/M_{\text{LE}})^2 - 1}{1 + (\gamma/2) M_{\text{TE}}^2} \tag{17}$$

For the present conditions ($t/c = 0.12$, $M_{\text{LE}} = 0.44$, $M_{\text{TE}} = 0.76$), we obtain $C_{D_h} = 0.116$ which matches exactly the computational result at $\alpha = 0°$.

It is important to realize that, when we add the vanes in the nozzle, the hydrostatic drag is largely *cancelled* by a redistribution of pressure on the nozzle walls. The small decline in C_p over the outer nozzle surface (Fig. 6b) creates a thrust force that is of the same magnitude as the hydrostatic drag of the vane. In the absence of entropy generation, cancellation is complete and the net drag is zero. The system drag (or net drag) we calculate here is the result of entropy generation due to viscous/wave effects generated by the airfoil.

The system drag coefficient still seems large compared to the drag coefficient of the external airfoil (0.024 versus 0.0044 at zero angle of attack). Recall, however, that we made an arbitrary decision to base the aerodynamic coefficients on the conditions of the leading edge ($M_{\text{LE}} = 0.44$). If we select the mid-chord conditions ($M_{\text{MID}} = 0.6$) for reference, the drag coefficients of the external airfoil and of the system become comparable, especially at the high angles of attack (Fig. 9). It is important to also consider vane-wall interference effects that can generate secondary losses. Roach and Turner [10] proposed the following relation for the drag increment due to secondary losses of support struts in gas turbine passages:

$$\Delta C_D = \frac{1.9}{\sqrt{1 - M^2}} \frac{t}{c} \frac{\delta_*}{h} \tag{18}$$

where M is the Mach number, t/c is the thickness-to-chord ratio, h is the span of the strut, and δ_* the average boundary layer displacement thickness on the two walls supporting the strut. In our case, the velocity profile approaching the vane, plotted in Fig. 10, has an average displacement thickness of 3 mm. Applying Eq. 18 to our vane, we obtain an increment $\Delta C_D = 0.005$. Considering the $\alpha = 0°$ case, if we add this increment to the drag coefficient of the external airfoil at $M = 0.6$, the total drag coefficient becomes 0.011 which is close to the system value of 0.012 shown in Fig. 9. Secondary losses can be mitigated by adding small fillets at the junction of the vanes with the nozzle walls [11].

Figure 11 plots the overall deflection angle of the bypass plume. The computed values are comparable to values measured in an ongoing experimental investigation of the mean velocity in the plume. Given the result of Fig. 7, the deflection angle is now easily predicted theoretically because the lift in Eq. 13 can be obtained directly from the $C_L - \alpha$ relation of the airfoil used. The deficit in nozzle mass flux is plotted in Fig. 12. Insertion of the vanes at $\alpha = 0°$ has insignificant impact on the mass flow rate. At the highest angle of attack, the mass flux deficit is 0.022%. The figure also shows the theoretical prediction based on the cosine of the plume deflection angle, assuming that the velocity profile at the exit is uniform in u and v. The computational result is in the same ballpark as the theoretical prediction.

The thrust loss for the bypass stream is plotted in Fig. 13. It starts at 0.04% with the vanes at $\alpha = 0°$ and reaches 0.10% for $\alpha = 8°$. For an engine with bypass ratio 5, the bypass stream produces about 77% of the total thrust, so the losses for the entire engine become 0.033% at $\alpha = 0°$ and 0.078% at $\alpha = 8°$ (Fig. 14) These losses appear quite acceptable from a performance point of view. Future works will address the losses under cruise conditions, but they are expected to also be very small. Refinement of the vane shape, using airfoil optimization techniques and possibly fillets at the wall junctions, holds the promise of even smaller thrust loss.

Conclusion

We examined computationally the flow field arising from the installation of airfoil-type vanes inside the bypass duct of a turbofan engine. The function of the vanes is to deflect the bypass plume for the purpose of noise reduction. This is a unique flow field where an airfoil is subjected to an externally-imposed favorable pressure gradient. The pressure gradient is shown to delay the onset of sonic flow on the airfoil. The lift curve slope matches that of the same airfoil in an infinite freestream when the lift

coefficient is based on the Mach number in the clean duct at the axial position of the leading edge of the vane. The lift of the entire system (comprising the nozzle walls and the vanes) is practically the same as the lift of the isolated vane. The drag coefficient of the isolated vane is large due to the axial pressure gradient acting across the airfoil length. This is counteracted by a reduced pressure on the internal nozzle walls, yielding a system drag coefficient comparable to that of an external airfoil when the reference Mach number is the Mach number in the clean duct at the vane mid-chord. The thrust loss of the bypass stream ranges from 0.04% with the vanes at zero angle of attack to 0.10% for vanes at 8° angle of attack. For an entire engine with bypass ratio of 5, the corresponding losses are approximately 0.03% and 0.08%. The vanes have an impact of less than 0.025% on the nozzle flow coefficient.

Acknowledgments

The support by NASA Glenn Research Center is gratefully acknowledged (Grant NAG-3-2345 monitored by Dr. Khairul B. Zaman and Dr. James Bridges). We also thank Dr. Mani Sadeghi for his guidance on the computations. The method and system of noise suppression via deflection of the bypass and/or core streams is proprietary to the University of California. U.S. Patent Pending.

References

[1] Papamoschou, D., "New Method for Jet Noise Suppression in Turbofan Engines," *AIAA Journal*, Vol. 42, No. 11, 2004, pp. 2245-2253.

[2] Papamoschou, D. and Nishi, K.A., "Jet Noise Suppression with Fan Flow Deflectors in Realistic-Shaped Nozzle," AIAA Paper 2005-0993, January 2005.

[3] Janardan, B.A., Hoff, G.E., Barter, J.W., Martens, S., Gliebe, P.R., Mengle, V., and Dalton, W.N., "AST Critical Propulsion and Noise Reduction Technologies for Future Commercial Subsonic Engines Separate-Flow Exhaust System Noise Reduction Concept Evaluation," NASA CR 2000-210039.

[4] Saiyed, N.H., Mikkelsen, K.L., and Bridges, J.E., "Acoustics and Thrust of Separate-Flow High-Bypass-Ratio Engines," *AIAA Journal*, Vol. 41, No. 3, 2003, pp. 372-378.

[5] Jameson, A., Schmift, W., and Turkel, E., "Numerical Solutions of the Euler Equations by Finite Volume Methods Using Runge-Kutta Time Stepping Schemes," AIAA Paper 81-1259, January 1981.

[6] Jameson, A. and Baker, T.J., "Improvements to the Aircraft Euler Method." AIAA Paper 87-0452, January 1987.

[7] Wilcox, D.C. "Reassessment of the Scale Determining Equation for Advanced Turbulence Models", *AIAA Journal*, Vol. 26, No. 11, 1988, pp. 1299-1310.

[8] Liu, F. and Zheng, X., "A Strongly Coupled Time-Marching Method for Solving the Navier-Stokes and k-ω Turbulence Model Equations with Multigrid," *Journal of Computational Physics,*, Vol. 128, No. 10, 1996.

[9] Jacobs, E.N., Ward, K.E., and Pinkerton, R.M., "The Characteristics of 78 Related Airfoil Sections from Tests in the Variable-Density Wind Tunnel," NACA Report 460, 1933.

[10] Roach, P.E. and Turner, J.T., "Secondary Loss Generation by Gas Turbine Support Struts," *International Journal of Heat and Fluid Flow,* Vol. 6, No. 2, June 1985, pp.79-88.

[11] Simpson, R.L., "Junction Flows," *Annual Review of Fluid Mechanics,* Vol. 33, January 2001, pp. 415-443.

Table 1 Grid for Clean Nozzle

Zone	Description	Dimensions
1	Inlet block	33x129x57
2	Midsection block	33x129x57
3	Midsection block	33x129x57
4	Exit block	33x129x57

Table 2 Grid for Nozzle with Vane

Zone	Description	Dimensions
1	C-grid (front)	33x113x57
2	C-grid (bottom/front)	45x129x57
3	C-grid (bottom/exit)	45x129x57
4	C-grid (top/front)	45x129x57
5	C-grid (top/exit)	45x129x57
6	Inlet grid (upstream)	29x65x57

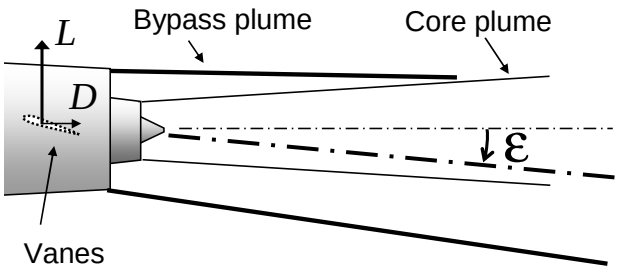

Fig. 1 General concept of Fan Flow Deflection.

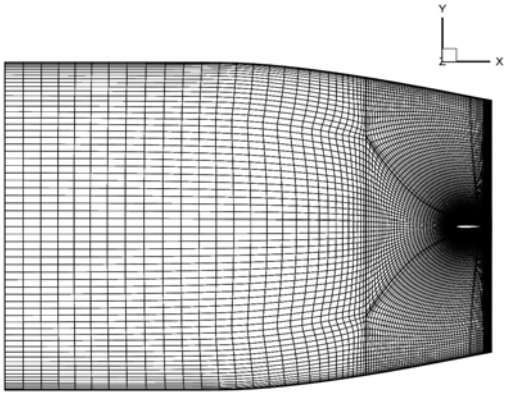

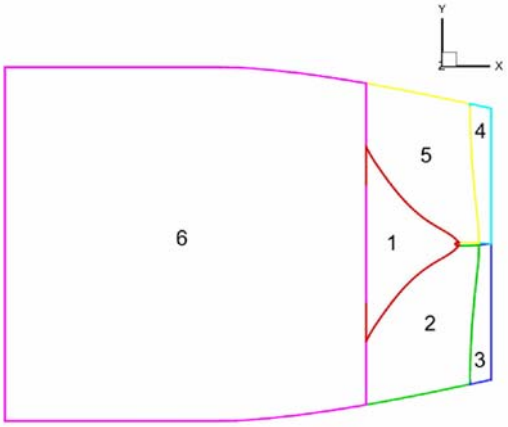

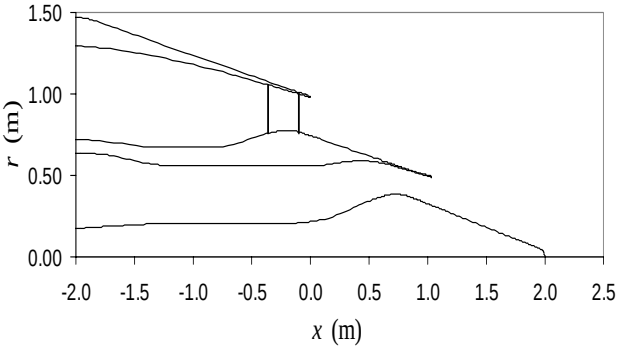

Fig. 2 Radial coordinates of nozzle showing placement of vanes

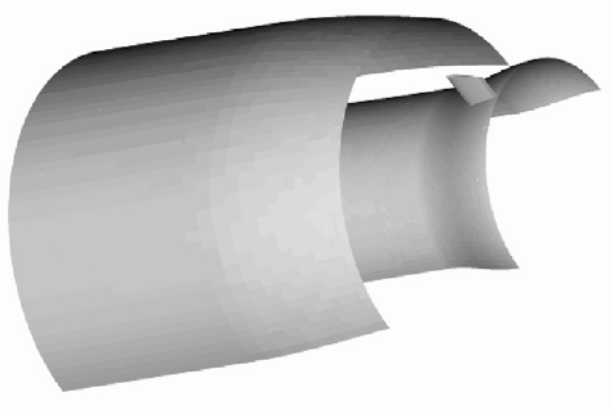

Fig. 3 Views of computational grid with mesh topology.

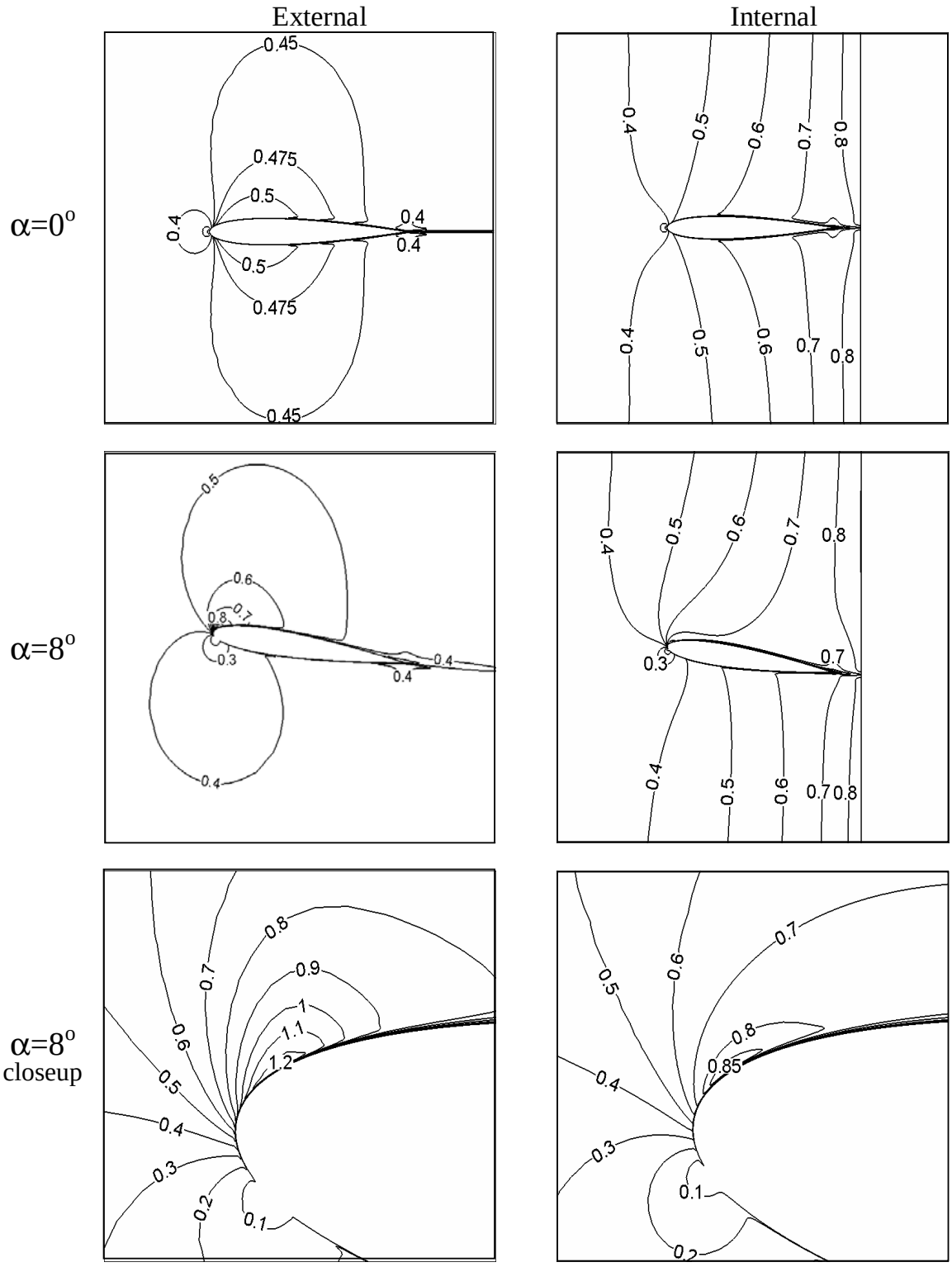

Fig. 4 Mach number contours for external airfoil (left column) and midplane of internal vane (right column) for angles of attack of 0 and 8 deg.

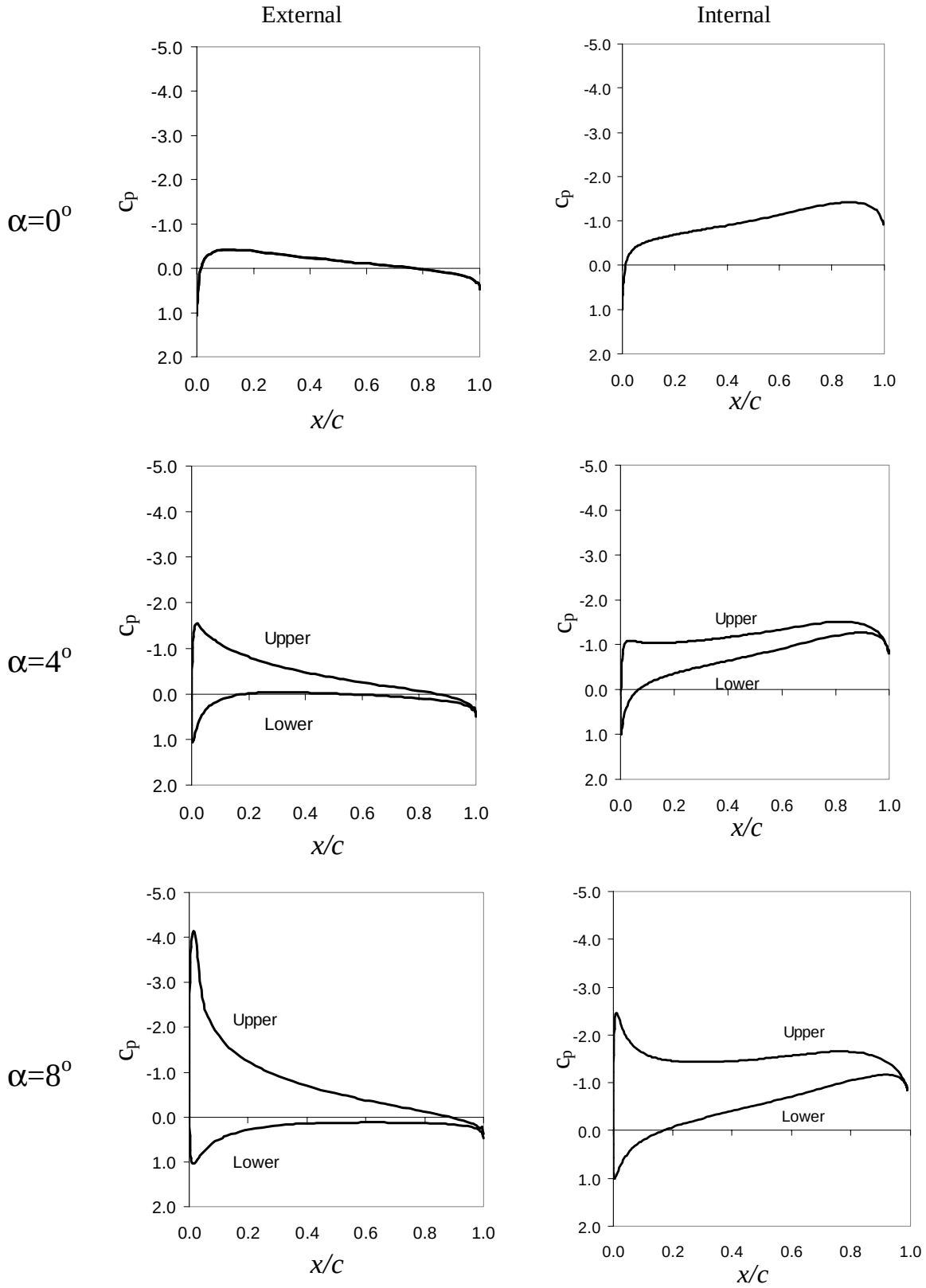

Fig. 5 Pressure coefficient for external airfoil (left column) and midplane of internal vane (right column) for angles of attack of 0, 4 , and 8 deg.

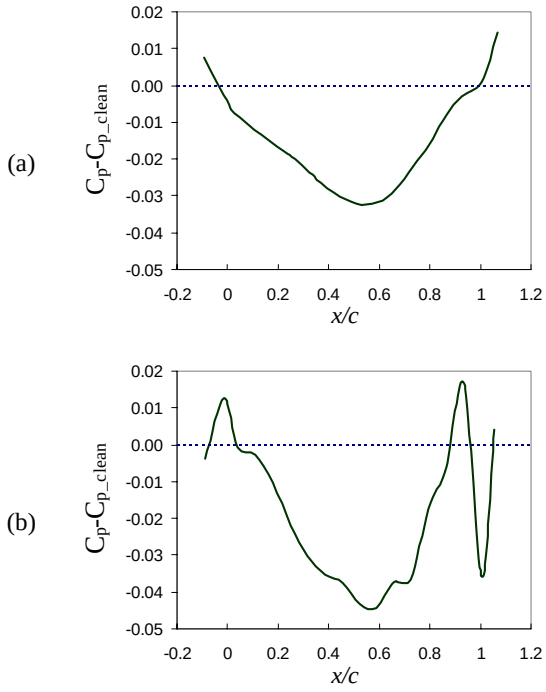

Fig. 6 Coefficient of circumferentially-averaged pressure on nozzle walls. Plotted is the difference between the case with vane at $\alpha = 0^\circ$ and the clean case. (a) Inner wall; (b) outer wall. x is referenced to the axial position of the vane leading edge.

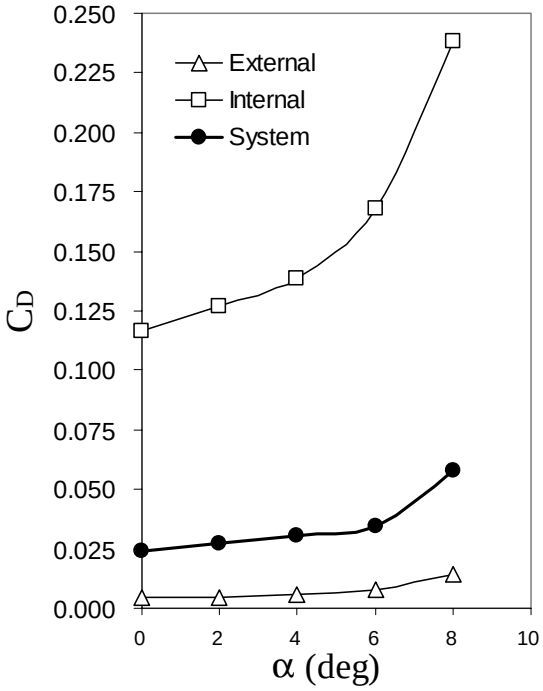

Fig. 8 Drag coefficient versus vane angle of attack. Reference conditions at vane leading edge.

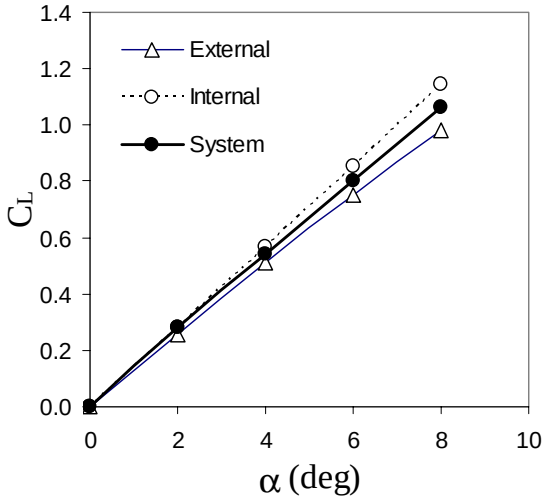

Fig. 7 Lift coefficient versus vane angle of attack. Reference conditions at vane leading edge.

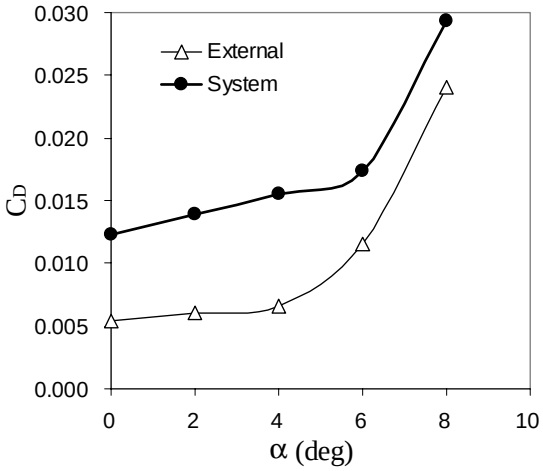

Fig. 9 Drag coefficient versus vane angle of attack for external airfoil and for system. Reference conditions at vane mid-chord.

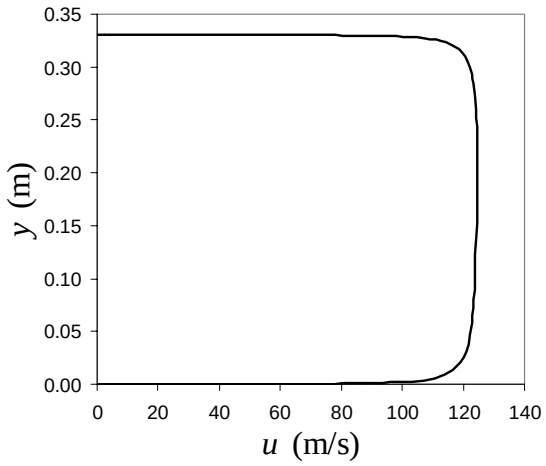

Fig. 10 Velocity profile in the duct one half chord length ahead of vane.

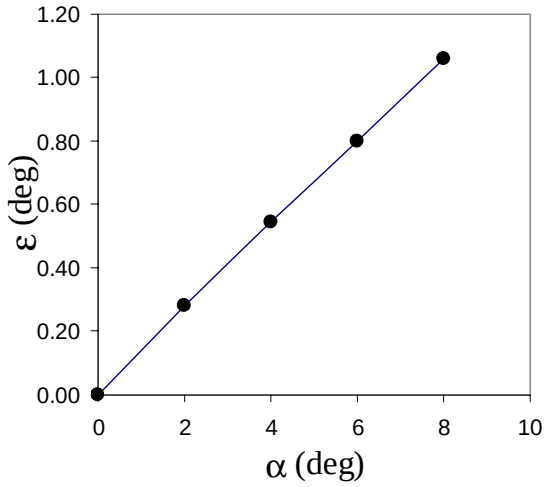

Fig. 11 Plume deflection angle versus vane angle of attack.

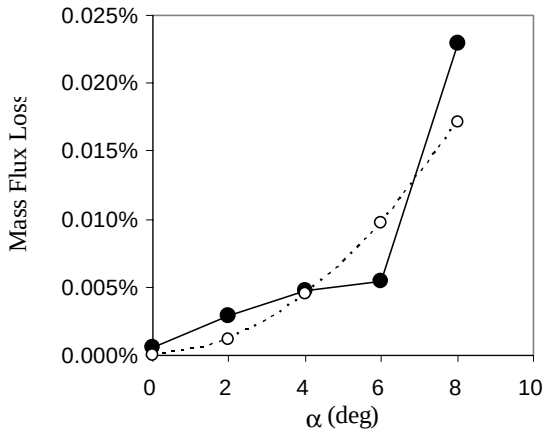

Fig. 12 Percent mass flux deficit versus vane angle of attack. Solid symbols: computation; open symbols: theory based on the cosine of the plume deflection angle.

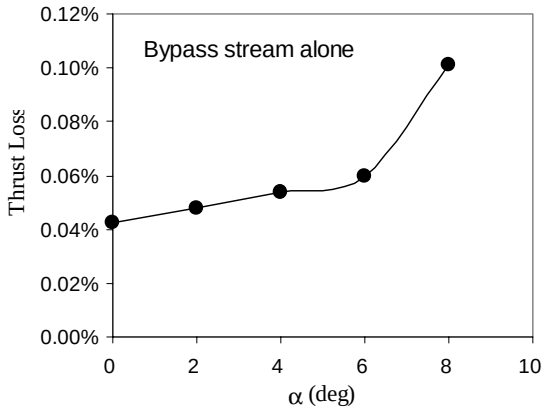

Fig. 13 Percent thrust loss of the bypass stream versus vane angle of attack.

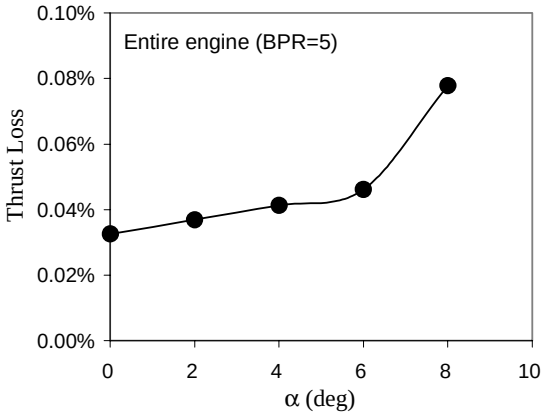

Fig. 14 Percent thrust loss of entire engine versus vane angle of attack.